Article

Not peer-reviewed version

Cu2O Nanoparticles as Nanocarriers and Its Antibacterial Efficacy

M. I. Torres-Ramos , Ubaldo de Jesús Martín Camacho , Suresh Ghotekar , Jorge Alberto Sánchez-Burgos , Oscar Arturo González-Vargas , Momoune Fellah , Alejandro Pérez-Larios *

Posted Date: 24 July 2024

doi: 10.20944/preprints202407.1818.v1

Keywords: Cu2O nanoparticles; Sol-gel method; Drug delivery; Functionalization; Mesoporous materials.

Article

Cu_2O Nanoparticles as Nanocarriers and Its Antibacterial Efficacy

M.I. Torres-Ramos [1], U.J. Martín-Camacho [1], J.A. Sánchez-Burgos [2], S. Ghotekar [3], O.A. González-Vargas [4], M. Fellah [5] and A. Pérez-Larios [1]*

[1] Nanomaterials, Water and Energy Research Laboratory, Department of Engineering, Centro Universitario de los Altos, University of Guadalajara, Tepatitlán de Morelos, Mexico
[2] Integral Food Research Laboratory, National Technological of Mexico/Technological Institute of Tepic, Tepic, Nayarit, Mexico.
[3] Centre for Herbal Pharmacology and Environmental Sustainability, Chettinad Hospital and Research Institute, Chettinad Academy of Research and Education, Kelambakkam 603103, Tamil Nadu, India.
[4] Departamento de Ingeniería en Control y Automatización, ESIME-Zacatenco, Instituto Politécnico Nacional, UPALM, Av. Politécnico s/n, Col., Zacatenco, Alcadía Gustavo A. Madero 07738, Ciudad de México, Mexico.
[5] Mechanical Engineering Department, ABBES Laghrour University, P.O 1252, 40004 Khenchela, Algeria.
* Correspondence: alarios@cualtos.udg.mx

Abstract: In this study, Cu_2O nanoparticles were synthesized using the sol-gel technique and subsequently functionalized with extracts from plants of the Rauvolfioideae subfamily and citrus fruits. Comprehensive characterization techniques, including UV-Vis spectroscopy, FT-IR, XRD, BET, SEM, and TEM, were employed to evaluate the structural and surface properties of the synthesized nanoparticles. The results demonstrated that both functionalized Cu2O nanoparticles exhibit mesoporous structures, as confirmed by nitrogen adsorption-desorption isotherms and pore size distribution analysis. The Green Extract functionalized nanoparticles displayed a more uniform pore size distribution compared to those functionalized with the natural extract. The study underscores the potential of these functionalized Cu_2O nanoparticles for applications in drug delivery, catalysis, and adsorption processes, highlighting the influence of the functionalization method on their textural properties and performance in antibacterial efficacy.

Keywords: Cu_2O nanoparticles; sol-gel method; drug delivery; functionalization; mesoporous materials

1. Introduction

The growing resistance of bacteria to traditional antibiotics has driven the search for new therapeutic strategies [1]. Among these, the controlled release of natural extracts via nanoparticles has emerged as a promising solution [2–4]. Cuprous oxide (Cu_2O) nanoparticles have garnered significant attention due to their unique properties, such as intrinsic antimicrobial activity, biocompatibility, and potential for sustained release of bioactive compounds[5,6].

Natural extracts, with their multiple bioactive compounds, offer an attractive alternative to synthetic antibiotics [7,8]. However, their efficacy can be limited by low solubility, stability, and bioavailability [9]. Incorporating these extracts into controlled release systems can significantly enhance their therapeutic activity by protecting them from degradation and allowing for sustained release at the site of action [10–12].

In this context, Cu_2O nanoparticles represent an innovative platform for the delivery of natural extracts. Their ability to interact with bacterial membranes, combined with the gradual release of bioactive compounds, can enhance the antibacterial efficacy of natural extracts [13,14]. Additionally, the use of Cu_2O allows for the exploration of synergies between the inherent antimicrobial properties of cuprous oxide and the therapeutic effects of natural extracts [15].

This study aims to evaluate the efficiency of Cu_2O nanoparticles as vehicles for the controlled release of natural extracts and determine their antibacterial efficacy. Through a series of experimental assays, the capacity of these nanoparticles to improve the stability and bioavailability of natural extracts, as well as their impact on bacterial growth inhibition, will be investigated.

 doi:10.20944/preprints202407.1818.v1

The research presented herein seeks not only to advance the understanding of Cu_2O nanoparticles' applications in drug delivery but also to provide a foundation for the development of new antibacterial therapies based on natural extracts, thereby contributing to the fight against bacterial resistance.

2. Results

In Figure 1, the micrographs of Cu_2O are observed. They present hexagon-shaped structures, characteristic of this material. These same morphologies can be seen under the polymeric coating applied in the functionalization. [16–18].

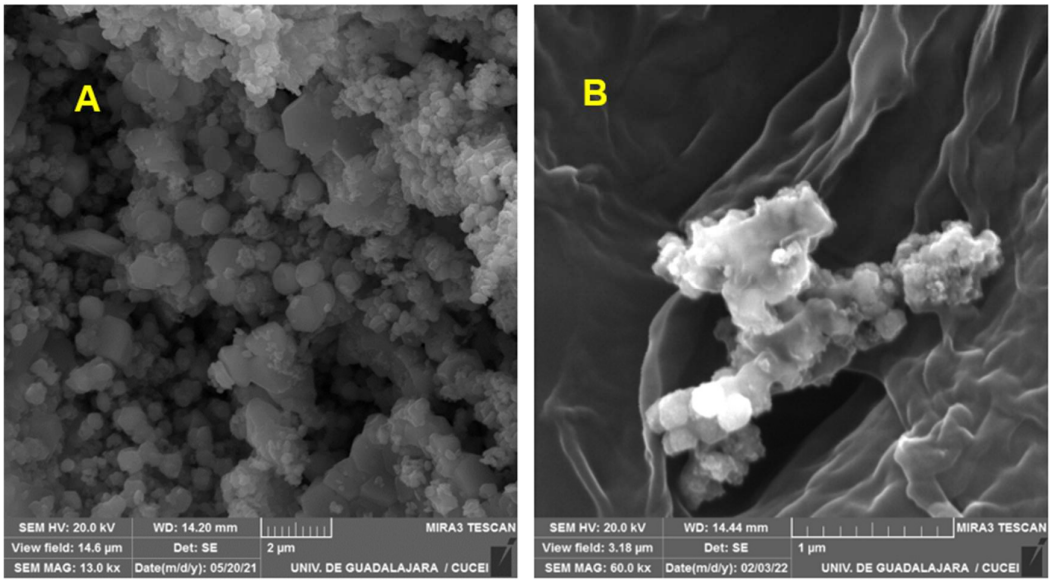

Figure 1. Micrografías de Cu_2O. A) Nanopartículas Cu_2O -N. B) Material funcionalizado.

In Figure 2 the XRD patterns of bare Cu_2O oxide are presented. The observed diffraction peaks correspond to the crystallographic planes (110), (111), (200), (220), (311), and (222), confirming the presence of Cu_2O in its face-centered cubic (FCC) phase [19]. The most intense peak, corresponding to the (111) plane, indicates a possible preferential orientation of the crystals in that direction [20]. The positions and relative intensities of the peaks are consistent with the expected values for Cu_2O in this crystal structure [21–23].

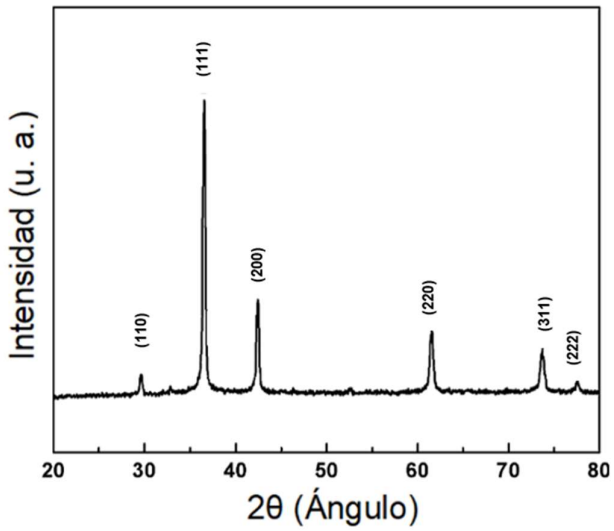

Figure 2. X-ray diffraction patterns of Cu_2O.

 doi:10.20944/preprints202407.1818.v1

The crystallite size, D, of the samples was estimated from the half width (b) of the peak at 2θ = 36° by the Scherrer formula: D = Kk/(b cos h) and the values are reported in Table 1. Crystallite size in the nanometer range (7.2–5.7 nm) was obtained in the sample [24].

Table 1. Comparative Analysis of MIC and MBCs of Functionalized NP's Against Various Pathogenic Bacteria.

	Listeria monocytogenes		***Enterococcus faecalis***		*Staphylococcus aureus*		*Salmonella paratyphi*		*Escherichia coli*	
	MIC	**MBC**	**MIC**	**MBC**	MIC	MBC	MIC	MBC	MIC	MBC
FM	80	160	40	60	40	640	40	640	80	320
FN	20	80	40	60	40	320	20	160	40	160

The most intense peak observed at approximately 2θ ≈ 36°, corresponding to the (111) plane, suggests that the Cu_2O nanoparticles have a preferential orientation in that direction [25]. This preferential orientation can influence the physical and chemical properties of the material, including its photocatalytic and antimicrobial activity. For instance, greater exposure of certain crystallographic planes can enhance the material's interaction with biological or catalytic agents [5,26].

Figure 3, shows a cluster of Cu_2O nanoparticles. The nanoparticles have an average size of 125 nm. The nanoparticles exhibit an irregular shape and appear to be agglomerated. The image provides an overview of the distribution and size of the nanoparticles [21,27].

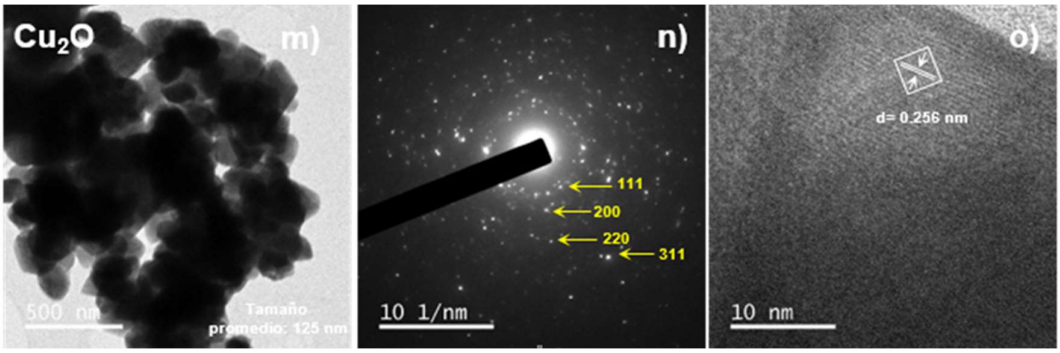

Figure 3. TEM Analysis of Cu_2O.

TEM images provide a detailed characterization of Cu_2O nanoparticles. The image (Figure 3a) confirms the size and morphology of the nanoparticles, showing a tendency to agglomerate, which is common in nanoparticles due to their high surface energy [28–30].

The electron diffraction pattern (Figure 3b) confirms the crystalline structure of the nanoparticles, corroborating the face-centered cubic (FCC) phase of Cu_2O, consistent with the results obtained from X-ray diffraction (XRD) [6,31]. The presence of well-defined rings indicates a high crystallinity of the nanoparticles [32].

The high-resolution (Figure 3c) provides an accurate measurement of the interplanar distances, which are important characteristics for identifying the crystalline structure [33]. The distance of 0.256 nm corresponds to the interplanar spacings of the (111) planes in the Cu_2O structure, further supporting the face-centered cubic phase [34–36].

Together, these samples confirm that the synthesized Cu_2O nanoparticles have a well-defined crystalline structure and morphological properties that may be suitable for applications in controlled drug release and antimicrobial activities.

Figure 4 shows the optical properties of CU_2O nanoparticles. In Figure 4a, the nanoparticles was measured over a wavelength range of 200 to 900 nm. Both samples exhibit strong absorbance in the UV-visible region, with significant absorption below 600 nm. Cu_2O-V shows a slightly higher absorbance at lower wavelengths (around 200-300 nm) compared to Cu_2O-N. The absorbance decreases as the wavelength increases for both samples, indicating a typical semiconductor absorption behavior [25,26]. The differences in absorbance between Cu_2O-V and Cu_2O-N might be due to variations in particle size, crystallinity, or surface properties [37]. In the other hand, Figure 4b shows the Tauc plots used to determine the band gap energies of Cu_2O-V and Cu_2O-N. The plot

 doi:10.20944/preprints202407.1818.v1

displays $(\alpha hv)^2$(\alpha hv)^2$(\alpha hv)^2$ versus energy (eV). The band gap for Cu_2O-V (black line) is determined to be 2.13 eV and for Cu2O N (red line) is determined to be 2.28 eV [38]. The band gap energies are slightly different between the two samples, suggesting variations in their electronic structure. The slight difference in band gap energies might be attributed to changes in particle size, defect states, or doping levels [39,40]. A higher band gap for Cu_2O-N indicates it might be more effective in applications requiring higher energy photons [41].

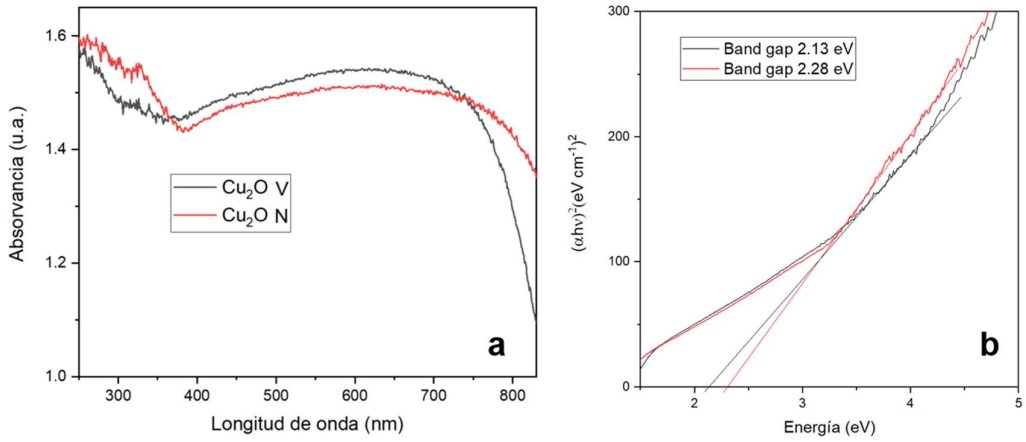

Figure 4. Spectrum of UV-Vis of Cu2O.

Figure 5, hows Fourier-transform infrared spectroscopy (FTIR) spectra for two samples: Cu_2O and PLGA-Cu_2O-Ext. The y-axis represents the percentage transmittance, while the x-axis represents the wavenumber in cm^{-1}, which corresponds to different vibrational modes of the molecules.

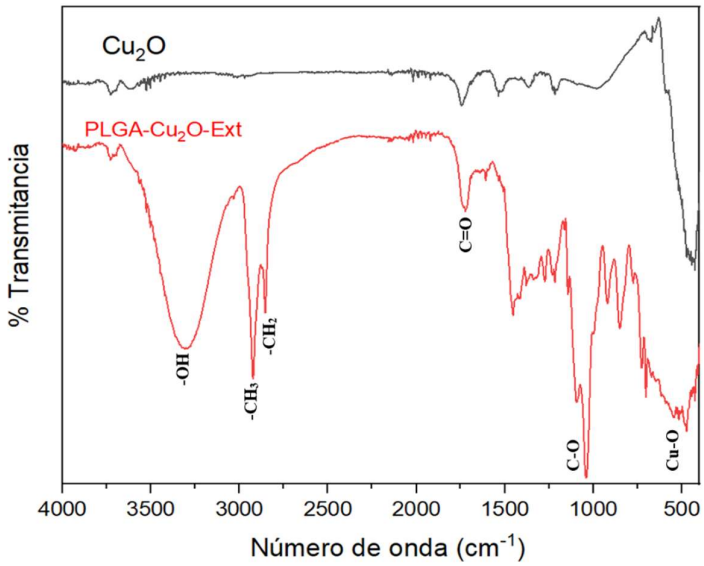

Figure 5. FTIR Spectra Comparison of Pure Cu_2O and PLGA-Coated Cu_2O NPs with Natural Extract.

The FTIR spectrum of Cu_2O shows distinct peaks that correspond to various vibrational modes associated with the material [21]. Around 600 cm^{-1}, this peak can be attributed to the Cu-O stretching vibration, characteristic of Cu_2O [42]. The spectrum does not show significant peaks in the higher wavenumber region, which is expected for pure Cu_2O as it lacks organic functional groups [30].

PLGA-Cu_2O-Ext Spectrum displays additional peaks, indicating the presence of organic functional groups and interactions between the components. Around 3500-3200 cm^{-1}, a broad peak corresponding to O-H stretching vibrations, indicating the presence of hydroxyl groups. Around 3000-2800 cm^{-1}, peaks corresponding to C-H stretching vibrations from $-CH_3$ and $-CH_2$ groups,

 doi:10.20944/preprints202407.1818.v1

suggesting the presence of aliphatic chains [43,44]. Around 1750-1700 cm^{-1}, a peak corresponding to C=O stretching vibrations, characteristic of carbonyl groups found in PLGA [45]. Around 1250-1000 cm^{-1}, peaks corresponding to C-O stretching vibrations, indicating ester functionalities in PLGA. Around 600 cm^{-1} [46], similar to the Cu_2O spectrum, indicating the presence of Cu-O stretching vibrations.

The Figure 6 shows nitrogen adsorption-desorption isotherms and corresponding pore size distribution plots (insets) for Cu_2O nanoparticles functionalized with two different extracts, labeled as (a) Green Extract (Cu_2O-VE) and (b) Orange Extract (Cu_2O-NE).

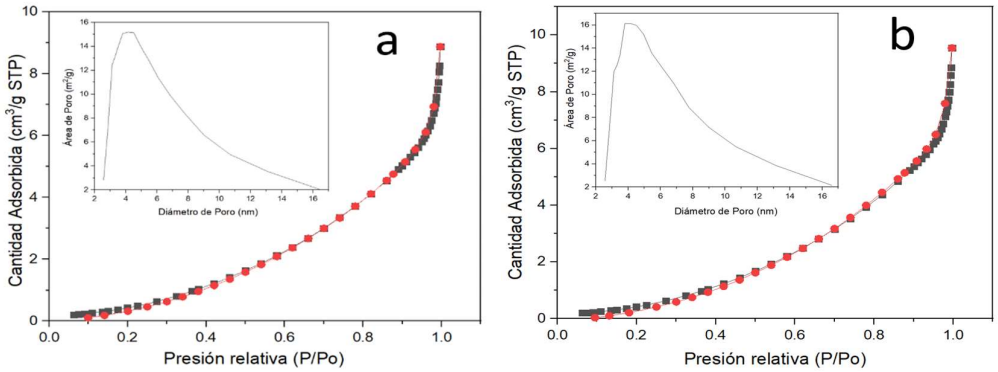

Figure 6. Nitrogen Adsorption-Desorption Isotherms and Pore Size Distribution of Cu_2O Nanoparticles Functionalized with Natural Extracts.

Both isotherms exhibit a typical Type IV shape according to the IUPAC classification, indicating the presence of mesoporous structures. The hysteresis loops observed at higher relative pressures (P/Po) are characteristic of capillary condensation in mesopores, suggesting the material's mesoporous nature. The amount of nitrogen adsorbed increases with relative pressure, indicating the progressive filling of mesopores.

The pore size distribution for both samples shows a significant peak in the mesopore range, around 4-10 nm. The peak height and width provide information about the pore volume and uniformity of the pore sizes. The Cu_2O-VE sample (Figure 6a) has a slightly narrower and more pronounced peak compared to Cu_2O-NE sample (Figure 6b), suggesting a more uniform pore size distribution for the Green Extract functionalized nanoparticles.

The Figure 7, showing the release profiles of natural extracts from Cu_2O nanoparticles at two different pH levels: 1.5 and 6.9. The figure with Cu_2O pH 1.5 shows control sample showing negligible release, as expected. FN sample shows the highest release rate, reaching about 45%, FM sample shows a moderate release rate, reaching around 35% and FV sample shows the lowest release rate among the experimental samples, reaching around 30% in 24 hours.

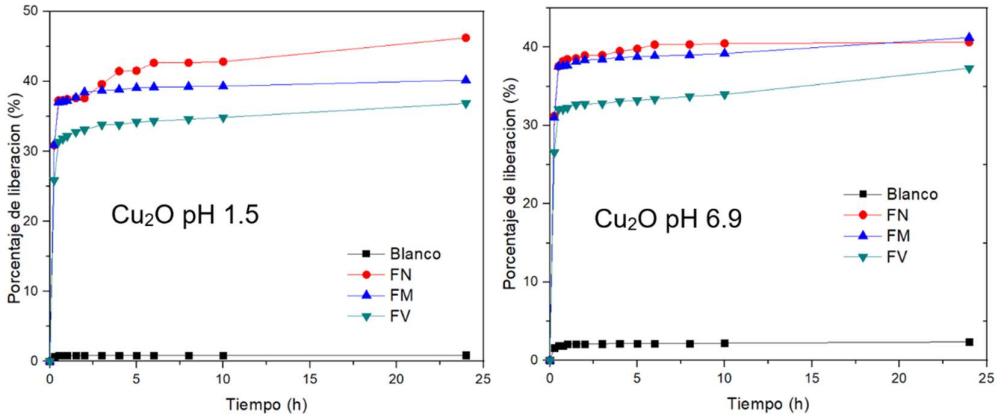

Figure 7. Release Profiles of Natural Extracts from Cu_2O NPs at Different pH.

 doi:10.20944/preprints202407.1818.v1

The highest release rate, reaching about 45%, the figure with Cu2O pH 6.9 shows a moderate release rate, reaching around 35% and this sample shows the lowest release rate among the experimental samples, reaching around 30%, all delivery samples was in 24 hours.

All samples (except the control) exhibit a rapid initial release within the first 5 hours, followed by a slower, sustained release up to 24 hours. The variation in release rates among FN, FM, and FV suggests different interactions or affinities between the natural extracts and the Cu_2O matrix.

The figure with Cu_2O pH 6.9 shows control sample showing negligible release, similar to the acidic pH condition. FN sample shows a high release rate, reaching about 40%, FM sample shows a moderate release rate, reaching around 35% and FV sample shows a lower release rate, reaching around 30%, all delivery was in 24 hours.

Similar to the acidic condition, all experimental samples show a rapid initial release, followed by a slower release. The release profiles are relatively consistent between the acidic and neutral pH, indicating that the Cu2O nanoparticles are stable and effective in controlling the release of natural extracts across a range of pH levels [47,48].

The evaluation was carried out to determine MIC and MBC of each of the functionalized materials and the results are presented below distributed in tables, remembering that for each material there are three functionalizations, FN with orange extract, FM involved the mixture of green extract and orange in equal parts and FV that only used green extract. The results of this last treatment will not be reflected in the tables since it did not present antibacterial activity in any of the materials, which is supported by other authors who attribute properties such as anti-inflammatory, neuroprotective, and even cognitive enhancers to the alkaloids, but They do not have sufficient antibacterial or antifungal activity to be considered antimicrobial agents.

The Table 1, provided lists the Minimum Inhibitory Concentrations (MIC) and Minimum Bactericidal Concentrations (MBC) of two types of functionalized nanoparticles (FM and FN) against five bacterial species: *Listeria monocytogenes*, *Enterococcus faecalis*, *Staphylococcus aureus*, *Salmonella paratyphi*, and *Escherichia coli*. These measurements are crucial in determining the antibacterial efficacy of the nanoparticles, where MIC indicates the lowest concentration that prevents visible growth of a bacterium, and MBC represents the lowest concentration at which the nanoparticles kill the bacteria.

2.1. Functionalized Nanoparticles FM

Shows variable efficacy across the bacterial strains. Notably effective against *Salmonella paratyphi* and *Escherichia coli* with an MIC of 40 µg/mL and 80 µg/mL respectively, and corresponding MBC values indicating a bactericidal effect at significantly higher concentrations. Exhibits a high bactericidal concentration for *Staphylococcus aureus* (640 µg/mL), suggesting a lower efficacy in completely killing the bacteria as compared to inhibiting its growth.

2.2. Functionalized Nanoparticles FN

Generally more effective than FM, with lower MIC values for *Listeria monocytogenes* and *Salmonella paratyphi* (20 µg/mL). Consistent MBC values for *Enterococcus faecalis* and relatively lower MBC values for other strains compared to FM, indicating a more potent bactericidal capability.

The varying responses of different bacteria to the same nanoparticles suggest that the mechanism of action could be influenced by the bacterial cell wall composition and the metabolic pathways of each species. For instance, Gram-positive bacteria like *Staphylococcus aureus* exhibit higher resistance to the bactericidal action of FM nanoparticles. FN nanoparticles demonstrate a more consistent and effective antibacterial activity both in terms of inhibition and bactericidal action across all tested bacteria. This could be attributed to differences in the surface properties, size, or the concentration of the active component in the FN formulation compared to FM. The data suggests that FN nanoparticles might be more suitable for broader applications in treating or preventing bacterial infections due to their lower MIC and MBC values. However, the specific application would need to consider the target bacterial infection and the local environment, as the effectiveness can vary. The relatively high concentrations needed for bactericidal action (especially noted in FM for *Staphylococcus aureus*) could contribute to the development of resistance. Continued monitoring and combination strategies might be necessary to mitigate such risks.

 doi:10.20944/preprints202407.1818.v1

This visual representation underscores the importance of determining the optimal concentrations and formulations for maximizing antibacterial activity while minimizing the risk of bacterial resistance development. Future studies should focus on understanding the mechanisms of action and further optimizing the nanoparticle formulations for specific applications.

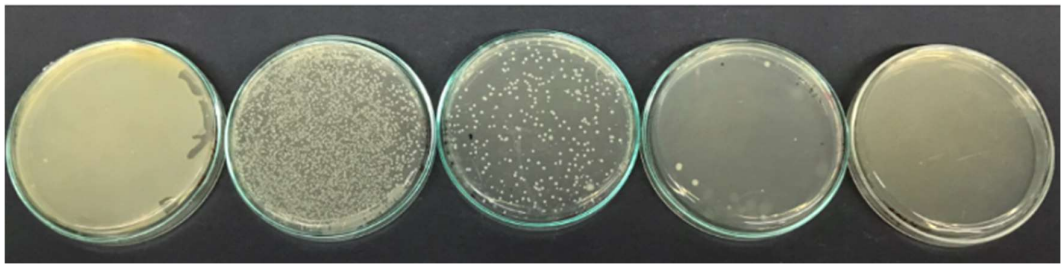

Figure 8. Evaluation on MBC agar plates.

3. Materials and Methods

Some characteristics of the extracts are protected because they are in the process of international patent approval with application No. PCT/IB2020/061916.

3.1. Synthesis of Nanoparticles

The materials of Cu_2O were prepared using a modified sol-gel synthesis [49]. Copper (II) nitrate were used as precursor (reagents obtained from Sigma-Aldrich Chemical Co., St. Louis, MO, USA). In a three-neck flask, 40 mL of extract was placed, and the precursor was added dropwise, maintaining a temperature of 70°C with constant stirring and under a vapor condensation system for 4 hours. Subsequently, the solution was transferred to a jacketed reactor at 0°C with stirring for 20 hours. The resulting xerogel was dried at 60°C, and the solid was ground in an agate mortar and then calcined at 500°C for 5 hours in a static air atmosphere with a heating rate of 2°C/min.

3.2. Functionalization of Nanoparticles

The nanoparticles (NPs) were functionalized using an organic phase containing ~5 mg of PLGA (75:25) and 400 µL of acetone, and an aqueous phase composed of 5 mL of a PVA solution (4%) and extracts (16% w/v). To this, 5 mg of nanomaterial was added and sonicated for 3 minutes. Subsequently, the phases were homogenized using an Ultra-turrax (IKA, T18; Germany), with the organic phase added dropwise. The resulting samples were then maintained at -80°C for 2 hours and lyophilized at -50°C (Labconco, FreeZone 6; Kansas, MO, USA) [50].

3.3. Characterization of Nanoparticles

Once the nanoparticles were obtained, it was necessary to determine their structural and surface characteristics. The size and distribution affect various properties and their potential applications; hence, it is essential to determine at least two main parameters once the nanoparticles are obtained.

The commonly used techniques to determine the structural and surface details of the synthesized nanoparticles include: UV-Vis spectroscopy, Fourier Transform Infrared Spectroscopy (FT-IR), X-Ray Diffraction (XRD), Nitrogen Physisorption (BET), and Scanning Electron Microscopy (SEM).

3.3.1. Scanning Electron Microscopy (SEM)

The morphology of the materials was observed using scanning electron microscopy (MIRA 3LMU, Tescan, London, UK) operated at 20 kV.

3.3.2. Transmission Electron Microscopy (TEM)

Samples were prepared for analysis by dispersing the nanoparticle powder, and a Philips model CM200 UT microscope was used, operated at 200 kV, with energy-dispersive X-ray spectroscopy (EDS).

 doi:10.20944/preprints202407.1818.v1

3.3.3. X-ray Diffraction (XRD)

Powder X-ray diffraction patterns were acquired using a Panalytical XRD diffractometer (Empyrean, Almelo, Netherlands) equipped with Cu Kα radiation (λ = 0.154 nm). Data were collected from 10° to 90° (2θ) with a scanning speed of 0.02°/0.2 s.

3.3.4. Nitrogen Physisorption (BET Method)

FT-IR spectra of the material were recorded with a Shimadzu FTIR spectrophotometer (IRTracer-100, Tokyo, Japan) using attenuated total reflectance (ATR) with a diamond waveguide (XR model). A standard deuterated triglycine sulfate (DTGS) detector with rapid recovery was used for the analysis. Spectra were recorded at room temperature, with 24 scans and 4 cm−1 resolution, ranging from 4000 cm−1 to 400 cm−1.

3.3.5. UV-Vis Spectroscopy

Absorption spectra of the materials were acquired using a Shimadzu UV-Vis spectrophotometer (UV-2600, Tokyo, Japan) equipped with an integrating sphere suitable for diffuse reflectance studies. UV-Vis spectra were analyzed at wavelengths from 190 to 900 nm [51].

The band-gap energy was calculated using the Tauc Plot method, as shown in equation 1:

$$(\alpha h\nu)^{\gamma} = A(h\nu - E_g) \qquad (1)$$

where α is the absorption coefficient, h is Planck's constant, v is the photon frequency, A is a proportionality constant determined by the refractive index, Eg is the band-gap energy, and the exponent γ denotes the nature of the electronic transition (γ=2 for a direct transition, γ=1/2 for an indirect transition).

3.3.6. Fourier Transform Infrared Spectroscopy (FT-IR)

This technique is based on measuring the absorption of electromagnetic radiation with wavelengths in the mid-infrared region, ranging from 4000 to 400 cm^{-1}. FT-IR has been employed to determine the characteristics of the synthesized NPs, providing spectral bands that reveal the presence of functional groups from organic and inorganic substances attached to the surface of the studied materials.

4. Conclusions

The synthesis and functionalization of nanoparticles via the sol-gel technique proved effective for Cu_2O. By utilizing specific precursors and maintaining controlled reaction conditions, we successfully produced nanoparticles with desired properties. The functionalization process, involving PLGA and PVA, allowed for the creation of stable nanomaterial systems, potentially enhancing their applicability in various fields.

Characterization techniques, such as UV-Vis spectroscopy, FT-IR, XRD, BET, SEM, and TEM, were crucial in determining the structural and surface properties of the synthesized nanoparticles. These methods provided detailed insights into the morphology, size distribution, surface chemistry, and crystalline structure, which are essential for understanding their behavior and potential applications.

SEM and TEM analyses revealed the morphology and detailed structure of the nanoparticles, while XRD confirmed their crystalline phases. FT-IR spectroscopy identified the presence of functional groups, indicating successful surface modification. UV-Vis spectroscopy and Tauc Plot analysis provided information on the optical properties and band-gap energies of the nanoparticles, crucial for applications in photocatalysis and other fields.

The provided MIC and MBC values highlight the potential of these functionalized nanoparticles as antibacterial agents against a spectrum of pathogenic bacteria. The consistent performance of FN suggests its suitability for further development and potential clinical applications. However, the variability in effectiveness underscores the need for tailored approaches depending on the specific bacterial strain and the clinical scenario. Future studies should explore the mechanisms of action to enhance the efficacy and reduce the potential for resistance.

Author Contributions: Writing—original draft preparation, T.-R. and M.-C.; methodology, P.-L.; formal analysis, S.-B.; writing—review and editing, S.G., M.F. and G.-V.; All authors have read and agreed to the published version of the manuscript.

Funding: This research received no external funding.

Institutional Review Board Statement: Not applicable.

Informed Consent Statement: Not applicable.

Acknowledgments: Torres-Ramos MI thank to Conacyt for the scholarships received (778183) and Sergio Oliva and Martin Flores from the UDG for the use of XRD and SEM equipment at the Centro Universitario de Ciencias Exactas e Ingenierias of the University of Guadalajara, Jalisco, Mexico.

Conflicts of Interest: The authors declare no conflicts of interest.

References

1. Medina-Palacios, S.E.; Vitales-Noyola, M.; López-González, E.; González-Amaro, A.M.; Méndez-González, V.; Pozos-Guillén, A. Root canal microorganisms and their antibiotic susceptibility in patients with persistent endodontic infections, with and without clinical symptoms. *Odontology* **2021**, *109*, 596–604, doi:10.1007/S10266-020-00580-2/FIGURES/3.
2. Elshafie, H.S.; Aliberti, L.; Amato, M.; De Feo, V.; Camele, I. Chemical composition and antimicrobial activity of chia (Salvia hispanica L.) essential oil. *Eur. Food Res. Technol.* **2018**, *244*, 1675–1682, doi:10.1007/s00217-018-3080-x.
3. Sharma, K.; Mahato, N.; Cho, M.H.; Lee, Y.R. Converting citrus wastes into value-added products: Economic and environmently friendly approaches. *Nutrition* 2017, *34*, 29–46.
4. Zangara, A. The psychopharmacology of huperzine A: an alkaloid with cognitive enhancing and neuroprotective properties of interest in the treatment of Alzheimer's disease. *Pharmacol. Biochem. Behav.* **2003**, *75*, 675–686, doi:10.1016/S0091-3057(03)00111-4.
5. Janczarek, M.; Endo, M.; Zhang, D.; Wang, K.; Kowalska, E. Enhanced Photocatalytic and Antimicrobial Performance of Cuprous Oxide/Titania: The Effect of Titania Matrix. *Materials (Basel).* **2018**, *11*, 2069, doi:10.3390/ma11112069.
6. Li, Y.; Chen, X.; Li, L. Facile thermal exfoliation of Cu sheets towards the CuO/Cu2O heterojunction: A cost-effective photocatalyst with visible-light response for promising sustainable applications. *RSC Adv.* **2019**, *9*, 33395–33402, doi:10.1039/C9RA06837F.
7. Babayevska, N.; Przysiecka, Ł.; Iatsunskyi, I.; Nowaczyk, G.; Jarek, M.; Janiszewska, E.; Jurga, S. ZnO size and shape effect on antibacterial activity and cytotoxicity profile. *Sci. Rep.* **2022**, *12*, doi:10.1038/S41598-022-12134-3.
8. Goldschmidt, G.M.; Krok-Borkowicz, M.; Zybała, R.; Pamuła, E.; Telle, R.; Conrads, G.; Schickle, K. Biomimetic in situ precipitation of calcium phosphate containing silver nanoparticles on zirconia ceramic materials for surface functionalization in terms of antimicrobial and osteoconductive properties. *Dent. Mater.* **2021**, *37*, 10–18, doi:10.1016/J.DENTAL.2020.09.018.
9. Perez-Cacho, P.R.; Rouseff, R.L. Fresh squeezed orange juice odor: A review. *Crit. Rev. Food Sci. Nutr.* 2008, *48*, 681–695.
10. Mobeen Amanulla, A.; Sundaram, R. Green synthesis of TiO2 nanoparticles using orange peel extract for antibacterial, cytotoxicity and humidity sensor applications. In Proceedings of the Materials Today: Proceedings; Elsevier Ltd, 2019; Vol. 8, pp. 323–331.
11. Krishnaraj, C.; Jagan, E.G.; Rajasekar, S.; Selvakumar, P.; Kalaichelvan, P.T.; Mohan, N. Synthesis of silver nanoparticles using Acalypha indica leaf extracts and its antibacterial activity against water borne pathogens. *Colloids Surfaces B Biointerfaces* **2010**, *76*, 50–56, doi:10.1016/j.colsurfb.2009.10.008.
12. Alarif, W.M.; Shaban, Y.A.; Orif, M.I.; Ghandourah, M.A.; Turki, A.J.; Alorfi, H.S.; Tadros, H.R.Z. Green Synthesis of TiO2 Nanoparticles Using Natural Marine Extracts for Antifouling Activity. *Mar. Drugs* **2023**, *21*, 62, doi:10.3390/MD21020062/S1.
13. Kuo, C.H.; Chen, C.H.; Huang, M.H. Seed-Mediated Synthesis of Monodispersed Cu2O Nanocubes with Five Different Size Ranges from 40 to 420 nm. *Adv. Funct. Mater.* **2007**, *17*, 3773–3780, doi:10.1002/ADFM.200700356.
14. Kandjani, A.E.; Sabri, Y.M.; Periasamy, S.R.; Zohora, N.; Amin, M.H.; Nafady, A.; Bhargava, S.K. Controlling Core/Shell Formation of Nanocubic p-Cu2O/n-ZnO Toward Enhanced Photocatalytic Performance. *Langmuir* **2015**, *31*, 10922–10930, doi:10.1021/ACS.LANGMUIR.5B01019/SUPPL_FILE/LA5B01019_SI_001.PDF.
15. Chen, L.; Zhang, Y.; Zhu, P.; Zhou, F.; Zeng, W.; Lu, D.D.; Sun, R.; Wong, C. Copper Salts Mediated Morphological Transformation of Cu2O from Cubes to Hierarchical Flower-like or Microspheres and Their Supercapacitors Performances. *Sci. Reports 2015 51* **2015**, *5*, 1–7, doi:10.1038/srep09672.

16. Huang, W.C.; Lyu, L.M.; Yang, Y.C.; Huang, M.H. Synthesis of Cu2O nanocrystals from cubic to rhombic dodecahedral structures and their comparative photocatalytic activity. *J. Am. Chem. Soc.* **2012**, *134*, 1261–1267, doi:10.1021/JA209662V.
17. Liang, C.; Li, X.; Han, J.; Ye, N.; Liu, H.; Feng, H.; Huang, L.; Liu, Y.; Peng, X. Hierarchical Cu/Cu2O structure derived from hexagonal Cu9S5 nanocrystal with enhanced electrocatalytic ability for hydrogen evolution reaction. *J. Alloys Compd.* **2021**, *883*, 160816, doi:10.1016/J.JALLCOM.2021.160816.
18. Ho, W.C.J.; Tay, Q.; Qi, H.; Huang, Z.; Li, J.; Chen, Z. Photocatalytic and Adsorption Performances of Faceted Cuprous Oxide (Cu2O) Particles for the Removal of Methyl Orange (MO) from Aqueous Media. *Mol. 2017, Vol. 22, Page 677* **2017**, *22*, 677, doi:10.3390/MOLECULES22040677.
19. Gao, Y.; Zhang, L.; van Hoof, A.J.F.; Hensen, E.J.M. On the surface-dependent oxidation of Cu2O during CO oxidation: Cu2+ is more active than Cu+. *Appl. Catal. A Gen.* **2020**, *602*, doi:10.1016/J.APCATA.2020.117712.
20. Babouri, L.; Belmokre, K.; Kabir, A.; Abdelouas, A.; Khettabi, R.; El Mendili, Y. Microstructure and crystallographic properties of Cu77Zn21 alloy under the effect of heat treatment. *Mater. High Temp.* **2019**, *36*, 165–172, doi:10.1080/09603409.2018.1499243.
21. Sudha, V.; Murugadoss, G.; Thangamuthu, R. Structural and morphological tuning of Cu-based metal oxide nanoparticles by a facile chemical method and highly electrochemical sensing of sulphite. *Sci. Rep.* **2021**, *11*, doi:10.1038/S41598-021-82741-Z.
22. Kuo, C.H.; Chen, C.H.; Huang, M.H. Seed-Mediated Synthesis of Monodispersed Cu2O Nanocubes with Five Different Size Ranges from 40 to 420 nm. *Adv. Funct. Mater.* **2007**, *17*, 3773–3780, doi:10.1002/ADFM.200700356.
23. Chen, L.; Zhang, Y.; Zhu, P.; Zhou, F.; Zeng, W.; Lu, D.D.; Sun, R.; Wong, C. Copper Salts Mediated Morphological Transformation of Cu2O from Cubes to Hierarchical Flower-like or Microspheres and Their Supercapacitors Performances. *Sci. Reports 2015 51* **2015**, *5*, 1–7, doi:10.1038/srep09672.
24. Dhonge, B.P.; Ray, S.S.; Mwakikunga, B. Electronic to protonic conduction switching in Cu2O nanostructured porous films: The effect of humidity exposure. *RSC Adv.* **2017**, *7*, 21703–21712, doi:10.1039/C7RA00383H.
25. Yu, Y.; Zhang, L.; Wang, J.; Yang, Z.; Long, M.; Hu, N.; Zhang, Y. Preparation of hollow porous Cu2O microspheres and photocatalytic activity under visible light irradiation. *Nanoscale Res. Lett.* **2012**, *7*, doi:10.1186/1556-276X-7-347.
26. Saad, N.A.; Dar, M.H.; Ramya, E.; Naraharisetty, S.R.G.; Narayana Rao, D. Saturable and reverse saturable absorption of a Cu2O–Ag nanoheterostructure. *J. Mater. Sci.* **2019**, *54*, 188–199, doi:10.1007/S10853-018-2811-5.
27. Dong, K.; He, J.; Liu, J.; Li, F.; Yu, L.; Zhang, Y.; Zhou, X.; Ma, H. Photocatalytic performance of Cu2O-loaded TiO2/rGO nanoheterojunctions obtained by UV reduction. *J. Mater. Sci.* **2017**, *52*, 6754–6766, doi:10.1007/S10853-017-0911-2.
28. Xiang, W.; Lei, M.; Wang, S.; Zhang, W.; Dong, Y. In-situ synthesis of ultrafine Cu2O nanoparticles onto MnO2 nanosheets for efficient non-enzymatic electrochemical sensing of hydrogen peroxide. *J. Appl. Electrochem.* **2023**, *53*, 1777–1785, doi:10.1007/S10800-023-01893-0/TABLES/1.
29. Badawy, S.M.; El-Khashab, R.A.; Nayl, A.A. Synthesis, characterization and catalytic activity of Cu/Cu2O nanoparticles prepared in aqueous medium. *Bull. Chem. React. Eng. Catal.* **2015**, *10*, 169–174, doi:10.9767/BCREC.10.2.7984.169-174.
30. Du, C.; Xiao, M. Cu2O nanoparticles synthesis by microplasma. *Sci. Reports 2014 41* **2014**, *4*, 1–5, doi:10.1038/srep07339.
31. Li, P.; Liu, L.; Qin, D.; Luo, C.; Li, G.; Hu, J.; Jiang, H.; Zhang, W. Cu2O concave hexapod microcrystals: selective facet etching and highly improved photocatalytic performance. *J. Mater. Sci.* **2019**, *54*, 2876–2884, doi:10.1007/S10853-018-3031-8.
32. Nethravathi, P.C.; Suresh, D.; Manjula, M. V.; Devaraja, S.; Mohan, S. Ag-Cu2O decorated reduced graphene oxide nanocomposite for photocatalytic water splitting, methylene blue dye degradation, electrochemical nitrite sensing, photoluminescence and selected biological applications. *Biomass Convers. Biorefinery* **2024**, *14*, 5711–5734, doi:10.1007/S13399-023-04922-2/FIGURES/18.
33. Sima, Z.; Ma, Z.; Song, P.; Wang, Q. Ultra-low concentration detection of NH3 using rGO/Cu2O nanocomposites at low temperature. *J. Mater. Sci. Mater. Electron.* **2021**, *32*, 22617–22628, doi:10.1007/S10854-021-06746-0.
34. Yuan, Z.; Zhang, Y.; Chen, H.; Xu, C. CTAB-assisted synthesis of eight-horn-shaped Cu2O crystals via a simple solution approach. *J. Mater. Sci. Mater. Electron.* **2018**, *29*, 4256–4260, doi:10.1007/S10854-017-8371-7.
35. Li, H.; Su, Z.; Hu, S.; Yan, Y. Free-standing and flexible Cu/Cu2O/CuO heterojunction net: A novel material as cost-effective and easily recycled visible-light photocatalyst. *Appl. Catal. B Environ.* **2017**, *207*, 134–142, doi:10.1016/J.APCATB.2017.02.013.

 doi:10.20944/preprints202407.1818.v1

36. Li, J.; He, M.; Yan, J.; Liu, J.; Zhang, J.; Ma, J. Room Temperature Engineering Crystal Facet of Cu2O for Photocatalytic Degradation of Methyl Orange. *Nanomaterials* **2022**, *12*, 1697, doi:10.3390/NANO12101697/S1.
37. Alegría, M.; Aliaga, J.; Ballesteros, L.; Sotomayor-Torres, C.; González, G.; Benavente, E. Layered Nanocomposite 2D-TiO2 with Cu2O Nanoparticles as an Efficient Photocatalyst for 4-Chlorophenol Degradation and Hydrogen Evolution. *Top. Catal.* **2021**, *64*, 167–180, doi:10.1007/S11244-020-01360-6.
38. Bouachma, S.; Ayouz-Chebout, K.; Kechouane, M.; Manseri, A.; Yaddadene, C.; Menari, H.; Gabouze, N. Synthesis of PSi-n/CuO-p/Cu2O-n heterostructure for CO2 gas sensing at room temperature. *Appl. Phys. A Mater. Sci. Process.* **2022**, *128*, doi:10.1007/S00339-021-05167-4.
39. Xia, Y.; He, Z.; Su, J.; Hu, K. Construction of novel Cu 2 O/PbBiO 2 Br composites with enhanced photocatalytic activity. *J. Mater. Sci. Mater. Electron.* **2019**, *30*, 9843–9854, doi:10.1007/S10854-019-01321-0.
40. Pellegrino, A.L.; Lo Presti, F.; Smecca, E.; Valastro, S.; Greco, G.; Di Franco, S.; Roccaforte, F.; Alberti, A.; Malandrino, G. A Low Temperature Growth of Cu2O Thin Films as Hole Transporting Material for Perovskite Solar Cells. *Materials (Basel).* **2022**, *15*, 7790, doi:10.3390/MA15217790/S1.
41. Babu, S.G.; Vinoth, R.; Praveen Kumar, D.; Shankar, M. V.; Chou, H.L.; Vinodgopal, K.; Neppolian, B. Influence of electron storing, transferring and shuttling assets of reduced graphene oxide at the interfacial copper doped TiO2 p–n heterojunction for increased hydrogen production. *Nanoscale* **2015**, *7*, 7849–7857, doi:10.1039/C5NR00504C.
42. Chinnaiah, K.; Maik, V.; Kannan, K.; Potemkin, V.; Grishina, M.; Gohulkumar, M.; Tiwari, R.; Gurushankar, K. Experimental and Theoretical Studies of Green Synthesized Cu2O Nanoparticles Using Datura Metel L. *J. Fluoresc.* **2022**, *32*, 559–568, doi:10.1007/S10895-021-02880-4.
43. Aseeri, J.; Alandis, N.M.; Mekhamer, W.; Alam, M. Miscibility studies of polystyrene/polyvinyl chloride blend in presence of organoclay. *Open Chem.* **2019**, *17*, 927–935, doi:10.1515/CHEM-2019-0095.
44. Apata, I.E.; Tawade, B. V.; Cummings, S.P.; Pradhan, N.; Karim, A.; Raghavan, D. Comparative Study of Polymer-Grafted BaTiO3 Nanoparticles Synthesized Using Normal ATRP as Well as ATRP and ARGET-ATRP with Sacrificial Initiator with a Focus on Controlling the Polymer Graft Density and Molecular Weight. *Mol. 2023, Vol. 28, Page 4444* **2023**, *28*, 4444, doi:10.3390/MOLECULES28114444.
45. Paneru, S.; Kumar, D. A Novel Electrochemical Biosensor Based on Polyaniline-Embedded Copper Oxide Nanoparticles for High-Sensitive Paraoxon-Ethyl (PE) Detection. *Appl. Biochem. Biotechnol.* **2023**, *195*, 4485–4502, doi:10.1007/S12010-023-04350-Y/TABLES/2.
46. Sadeghi-Avalshahr, A.; Nokhasteh, S.; Molavi, A.M.; Khorsand-Ghayeni, M.; Mahdavi-Shahri, M. Synthesis and characterization of collagen/ PLGA biodegradable skin scaffold fibers. *Regen. Biomater.* **2017**, *4*, 309–314, doi:10.1093/RB/RBX026.
47. Długosz, O.; Lis, K.; Matyjasik, W.; Radomski, P.; Pulit-Prociak, J.; Banach, M. Cu2O Nanoparticles Deposited on Y2O3 and CuO: Synthesis and Antimicrobial Properties. *J. Clust. Sci.* **2023**, *34*, 2153–2165, doi:10.1007/S10876-022-02375-7/FIGURES/6.
48. Wan, F.; Bohr, A.; Maltesen, M.J.; Bjerregaard, S.; Foged, C.; Rantanen, J.; Yang, M. Critical solvent properties affecting the particle formation process and characteristics of celecoxib-loaded PLGA microparticles via spray-drying. *Pharm. Res.* **2013**, *30*, 1065–1076, doi:10.1007/S11095-012-0943-X.
49. Pérez-Larios, A.; Torres-Ramos, I.; Zanella, R.; Rico, J.L. Ti-Co mixed oxide as photocatalysts in the generation of hydrogen from water. *Int. J. Chem. React. Eng.* **2021**, *0*, doi:10.1515/IJCRE-2021-0049.
50. Torres-Ramos, M.I.; Martín-Marquez, M.F.; Leal-Moya, M.D.C.; Ghotekar, S.; Sánchez-Burgos, J.A.; Pérez-Larios, A. PLGA-TiO2 as a Carrier System for Drug Release. *Int. J. Mol. Sci. 2022, Vol. 23, Page 10755* **2022**, *23*, 10755, doi:10.3390/IJMS231810755.
51. A.; Marizcal-Barba, A.; Limón-Rocha, I.; Barrera, A.; Eduardo Casillas, J.; González-Vargas, O.A.; Luis Rico, J.; Martinez-Gómez, C.; Pérez-Larios, A. TiO2-La2O3 as Photocatalysts in the Degradation of Naproxen. *Inorganics 2022, Vol. 10, Page 67* **2022**, *10*, 67, doi:10.3390/INORGANICS10050067.